# Modelling diffractive effects in silicon pore optics for the ATHENA X-ray Telescope

D. Spiga, G. Sironi, D. Della Monica Ferreira, A. Jegers, E. Bergbäck Knudsen, et al.

D. Spiga, G. Sironi, D. Della Monica Ferreira, A. S. Jegers, E. Bergbäck Knudsen, M. Bavdaz, I. Ferreira, "Modelling diffractive effects in silicon pore optics for the ATHENA X-ray Telescope," Proc. SPIE 12181, Space Telescopes and Instrumentation 2022: Ultraviolet to Gamma Ray, 121814J (31 August 2022); doi: 10.1117/12.2628133

SPIE.

Event: SPIE Astronomical Telescopes + Instrumentation, 2022, Montréal, Québec, Canada

# Modelling diffractive effects in silicon pore optics for the ATHENA X-ray telescope

D. Spiga*, G. Sironi
*INAF-Osservatorio Astronomico di Brera, Via E. Bianchi 46, 23807 Merate (Italy)*

D. Della Monica Ferreira, A.′S Jegers, E. Bergbäck Knudsen
*Technical University of Denmark (DTU), Juliane Maries Vej 30, DK-2100 Copenhagen (Denmark)*

M. Bavdaz, I. Ferreira
*European Space Agency (ESA), Keplerlaan 1, 2201 AZ Noordwijk (Netherlands)*

## ABSTRACT

Silicon Pore Optics (SPO) are the technology selected for the assembly of the mirror module of the ATHENA X-ray telescope. An SPO mirror module consists of a quadruple stack of etched and wedged silicon wafers, in order to create a stiff and lightweight structure, able to reproduce in each pore the Wolter-I geometry required to image X-rays on the telescope focal plane. Due to the small pore size (a few $mm^2$), aperture diffraction effects in X-rays are small, but not totally negligible to the angular resolutions at play. In contrast, diffraction effects are the dominant term in the UV light illumination that will be used to co-align the 600 mirror modules of ATHENA to a common focus. For this reason, diffractive effects need to be properly modeled, and this constitutes a specific task of the ESA-led SImPOSIUM (SIlicon Pore Optic SImUlation and Modelling) project, involving INAF-Brera and DTU. In this context, a specific software tool (SWORDS: SoftWare fOR Diffraction of Silicon pore optics) has been developed to the end of simulating diffraction effects in SPO mirror modules. This approach also allows the user to effectively predict the effects of various imperfections (figure errors, misalignments) in a self-consistent way, in different experimental configurations (X-ray source off-axis or at finite distance), as a fast and reliable alternative to ray-tracing, also at X-ray wavelengths.

**Keywords:** SWORDS, SImPOSIUM, diffraction, silicon pore optics, wave optics

## 1. INTRODUCTION

Even if the propagation of X-rays through a system of grazing-incidence mirrors is usually and successfully treated using ray-tracing techniques, one should always bear in mind that X-rays are electromagnetic waves, not traveling corpuscles, and that their propagation is ruled by Maxwell laws. Therefore, the truly correct approach to the interaction of X-rays with a reflective surface is represented by wave optics. Aperture diffraction, arising when attempting to "crop" a light wavefront at the aperture edges of an optical system, and X-ray scattering, resulting from phase alteration in a wavefront reflected by a rough mirror surface, are manifestations of the wave nature of X-rays, and a basic consequence of Heisenberg's uncertainty principle also. Application of geometric optics to these situations would return results in net contrast with the reality. Fortunately, geometric optics *does* return accurate results whenever the X-ray wavelength $\lambda$ is orders of magnitude smaller than *both* the apertures at play, which is usually the case, and the mirror imperfections projected on the incident wavefront, a situation met only in the absence of surface roughness. These conditions can be replaced by the equivalent statement that the slope error rms be much greater than the dimensions of the diffraction-limited focal spot. Unfortunately, there is no *a-priori* separation between mirror figure errors, roughness, and the "mid-frequencies" that can be - somehow questionably - identified in the centimeter-millimeter regime of spatial wavelengths in the power spectrum of profile imperfections. This makes the realm of applicability of geometric optics uncertain to some extent.

In the recent past, we have dedicated papers to prove that wave optics can consistently account for all these effects, including the nonidealities of X-ray mirrors at *all* the spatial scales. We have found that the Fresnel integrals

* corresponding author: daniele.spiga@inaf.it, phone +39-0272320-427

Space Telescopes and Instrumentation 2022: Ultraviolet to Gamma Ray, edited by Jan-Willem A. den Herder, Shouleh Nikzad, Kazuhiro Nakazawa, Proc. of SPIE Vol. 12181, 121814J · © 2022 SPIE · 0277-786X · doi: 10.1117/12.2628133

describing the construction of a reflected/diffracted/scattered wavefront can be significantly simplified in one dimension by collapsing the computation into the incidence plane, and neglecting deviations in the azimuthal direction.[1] The results have returned excellent agreement with experimental results,[2] and the WISE code implementing this formalism has become a part of the OASYS simulation package.[3] In this paper, we discuss some applications of wave optics to model the imaging properties of Silicon Pore Optics (SPO), the technology being selected for assembling the ATHENA X-ray telescope, in order to fulfill both requirements of a large aperture (2.5 m) and an angular resolution of 5 arcsec half-energy width (HEW) keeping the mass-to-area ratio as low as possible.[4] SPOs are obtained from silicon wafers etched on their non-optical side in order to form parallel grooves with rectangular sections.[5] At the *cosine* company (Warmond, the Netherlands), these wafers are properly diced, wedged, coated and stacked onto a mandrel to endow the polished and reflective optical surfaces with focusing and co-focal curvatures. The resulting stack is an array of narrow channels, which are properly dimensioned to optimize the collection area and the stiffness of the focusing profiles. Four stacks (two XOUs in parallel, see Figure 1) reproduce the widespread parabola-hyperbola (Wolter-I) focusing geometry and constitute an SPO mirror module (MM). The ATHENA X-ray telescope optics comprises 600 X-ray MMs of 12 m focal length, that need to be co-focally integrated into a 6-petal supporting structure. After manufacturing, the MMs have to be qualified at the BEaTriX X-ray facility,[6] to be subsequently aligned under illumination at 218 nm in the UVOB facility[7] at the premises of the Medialario company (Bosisio Parini, Italy), and finally calibrated in the nearby VERT-X facility.[8]

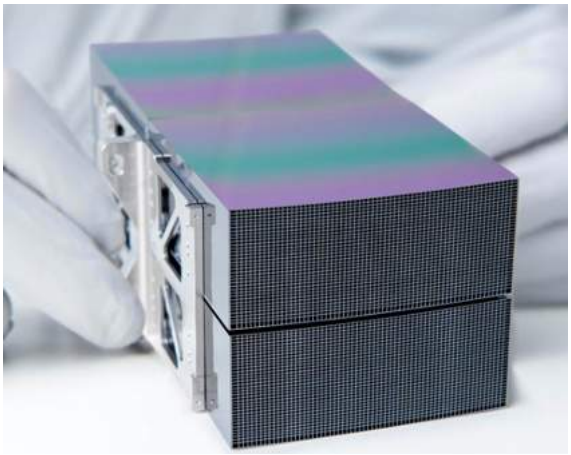

*Figure 1. An SPO mirror module (image credits: ESA) consists of two Wolter-I double stacks with 38 plate pairs each. A typical pore pitch is 2.3 mm, while the current pore height is 665 µm. The mirror membrane is 170 µm thick, while the rib width can be constant (also 0.17 mm thick) or, for the inner mirror modules, variable along the plate width to ease the rib alignment.*

To predict the optical performance of SPO MM and of the full mirror assembly of ATHENA, INAF-OAB and DTU are engaged in the ESA-led SImPOSIUM (SIlicon Pore Optic SImUlation and Modelling) project.[9] Performance simulation are carried out on two fronts: for the full mirror assembly, ray-tracing is the only viable option and a powerful tracing program (SPORT, Silicon Pore Optics Ray-tracing Tool) was developed to this specific end.[10],[11] On the other front, the optical performances of single MMs can be modelled using wave optics functionalities implemented in SWORDS (SoftWare fOR Diffraction Simulation of silicon pore optics): the first widget-based application aimed at the simulation of the diffraction effects in SPO MMs, from UV light to soft X-rays. Just like SPORT, SWORDS is a flexible, user-friendly, graphical user interface program. The open source code can be run in IDL under any operative system. Moreover, the current release 3.7.2 also comes as a stand-alone executable package for MacOS or Windows. The full SWORDS package is freely available[1] along with a detailed user manual.[12]

The motivation for modelling diffractive effects in SPOs is twofold. First, a point spread function (PSF) simulation using geometric optics may become inaccurate as the SPO technology moves forward and the achievable angular resolution constantly improves.[5] For example, undulations in the tangential profile behave as a grating when their amplitude is reduced below a certain value, and wave optic simulations become mandatory to obtain reliable results; additionally, not only the separation of the spatial scales obeying geometric/physical optics can be arbitrary, but also mixing PSFs resulting from the different treatments is also affected by a high level of uncertainty. A formalism

[1] https://drive.google.com/drive/folders/1mCqlS0DCEJxqqo_VYmQNlQqyNaiqE5UD

entirely based on wave optics, in contrast, removes all the ambiguities: all the spectral ranges of mirror defects, including mid-frequencies, are treated comprehensively, returning a single PSF at that specific value of λ, in which each spectral regime takes on the correct relevance.

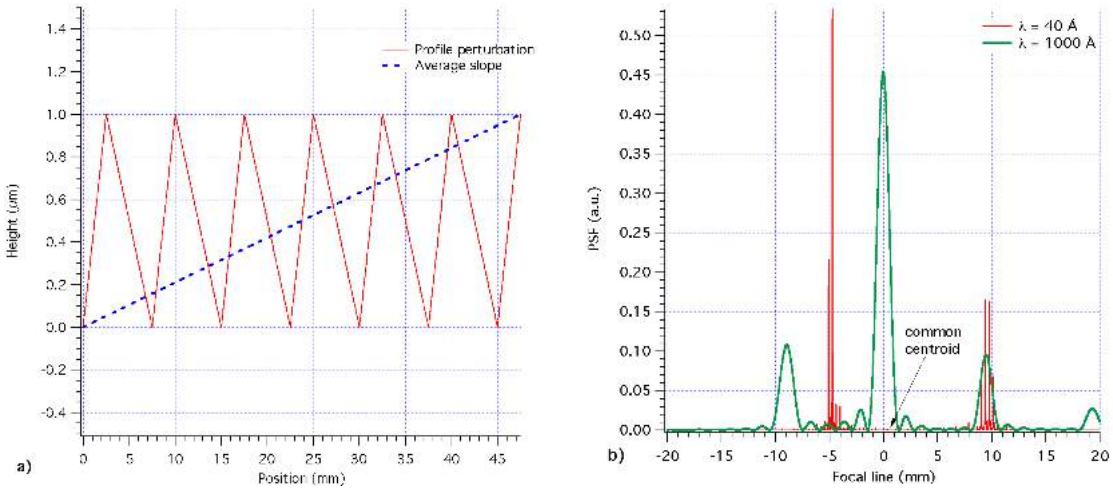


*Figure 2. Left: An asymmetric figure error in the mid-frequency range. Right: The PSF computed in UV light (λ = 100 nm) and X-rays (λ = 1 nm). Both PSFs were computed using the WISE code.[1] As expected, the centroid was displaced near x = 1 mm. Even if the perturbation has a much higher relevance at high energy, and therefore two PSFs look completely different in the two cases, the centroid position is the same.*

Secondly, a reliable prediction of the diffraction pattern in UV is a crucial activity for the alignment of SPO MMs in ATHENA. Indeed, more than previous types of optical concepts used in X-ray optics, SPO mirror modules are characterized by high density of obstructing structures, i.e., ribs (oriented radially) and membranes (along the azimuth) to endow the modules with the required stiffness. Due to the small value of λ, this would limit the angular resolution only negligibly,[13] i.e., at 0.5 arcsec level at 1 keV, which is far better than the requirement for ATHENA (5 arcsec HEW). However, aperture diffraction plays a major role when an MM aperture is illuminated in UV light for alignment purposes. The problem of assembling a large number of MMs, ensuring their co-focality, should not be underestimated. Aiming at a final HEW of < 5 arcsec for the final assembly, the foci of all the optical assembly in ATHENA should coincide to within < 1 arcsec. Aligning the foci in X-rays seems hardly viable, because of the need to operate in high vacuum and employing a highly-collimated X-ray beam of 2.5 m in diameter. In contrast, UV light can be used in air and easily folded into a compact space using planar mirrors. The price to pay is a higher level of aperture diffraction that overwhelms the focal spot by orders of magnitude, making the quest for the focus uncertain at first glance. Nevertheless, this alignment technique has been fruitfully used in assembling and aligning a number of X-ray mirrors in optical modules such as XMM's and eROSITA's,[14] taking as reference the *centroid* (or barycenter) of the UV focal spot, which can be experimentally located to high accuracy, and assuming it to reliably mark the location of the focus also under X-ray illumination. This should not be taken for granted, because the response of the PSF to a perturbation of given frequency depends on λ; therefore, it can *completely* change from UV to X-rays (Figure 2), and the profile asymmetries might *in principle* be inherited by the PSF to different extents, causing different displacements of the centroid. Fortunately, this is not the case. Even if the two PSFs completely differ from each other, their centroids actually stay at the same location. In addition, the centroid approach was verified in the ASPHEA project,[15] by testing an integrated optical module, firstly in the UVOB and later in X-rays at PANTER. In the context of the SImPOSIUM and ASPHEA activities, this concept has also been validated experimentally (Figure 3), through diffraction simulations on- and off-axis vs. measurements in the UVOB, so as to corroborate the centroid measured in UV as a reliable marker of the expected focal spot in X-rays, also for a complex structure such as an SPO's.[16] At this regard, an analytical proof of the centroid coordinate invariance with λ can be provided too: for the reader interested in mathematical details, it is deferred to Appendix A of this paper.

In this work, we present the functionalities of SWORDS and its implementation of the diffraction formula in Fresnel, single diffraction approximation, which enabled us to return accurate modelling of the 2D focus without exceeding a certain computation intensiveness. As of today, SWORDS can only simulate single SPO MMs, providing a viable alternative to ray-tracing, especially when the conditions for the application of geometric optics are not met. An extension to systems of MMs is foreseen in the next future.

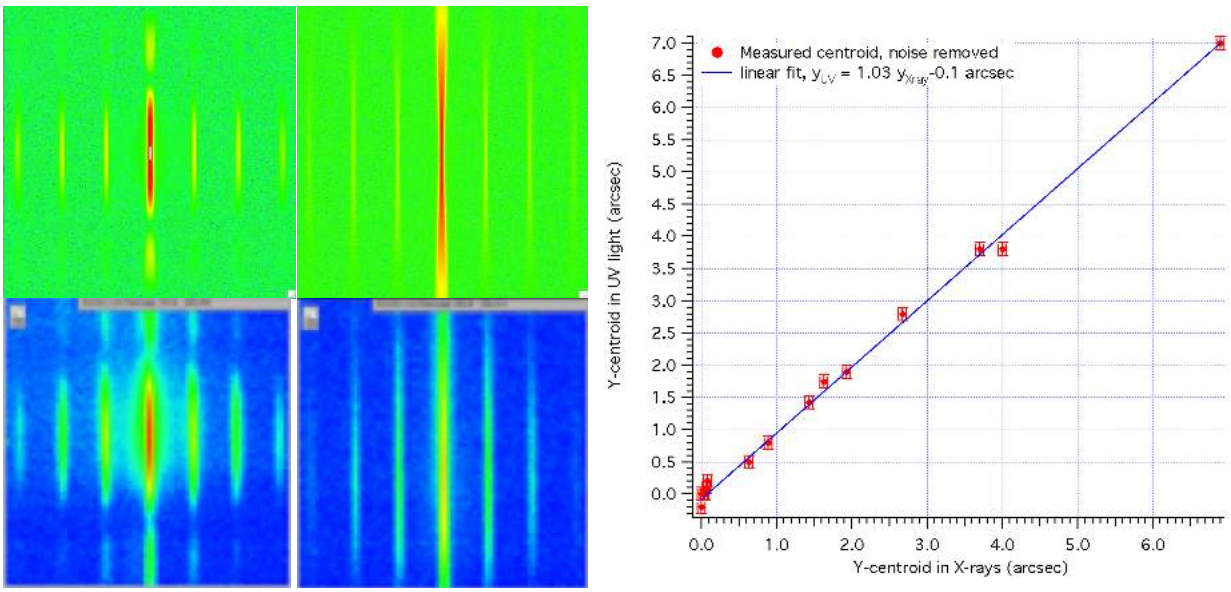


*Figure 3. Left: comparison between simulated (top) and measured in the Medialario UVOB (bottom) diffraction patterns at 218 nm of an SPO MM on-axis. Center: the same comparison, for the same module 11 arcmin off-axis. Right: agreement between the centroid vertical coordinate, as simulated in UV light vs. in X-rays (after[16]).*

## 2. DIFFRACTION FROM AN SPO MM IN FRESNEL APPROXIMATION

Unlike its 1D relative, a 2D exact treatment of the Fresnel diffraction often poses a heavy computation load. However, it is well known that a considerable simplification is represented by the *Fresnel approximation*, which is applicable when the image is observed at a distance $D$ from the diffracting object much larger than its linear width, $W$, and height, $H$. Figure 4 shows that this condition is well met in our case, if the observation plane is not too close to the module. Now, because the nominal Wolter-I profile focuses a parallel beam at a distance $f$, it is easily shown[17] that the Fresnel diffraction can be computed via a Fourier Transform, where the quadratic terms of the optical path difference (OPD) have been cancelled by the Wolter-I focusing properties. This allows us to state, indeed, that the condition $D > 2W^2/\lambda$ for the application of the far-field approximation is unnecessary in our case; therefore, the range of applicability of SWORDS is much wider than it would seem at first glance. By the way, we have already successfully used the Fresnel approximation to simulate the collimator of the VERT-X calibration facility.[18]

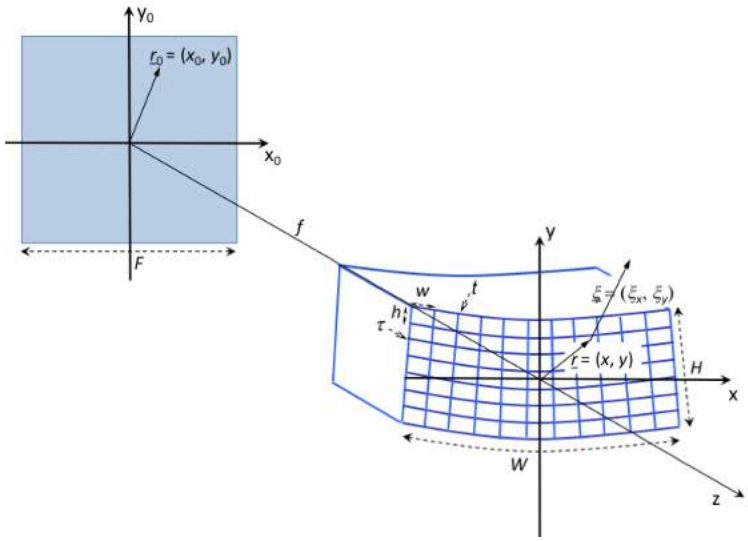


*Figure 4. Schematic of the diffraction from an SPO module. The SPO MM aperture and the observation plane are described via the coordinates (x, y) and ($x_0$, $y_0$) respectively. A displacement on the aperture pupil is denoted by ($\xi_x$, $\xi_y$).*

If we further assume the incident beam uniform, monochromatic, and spatially coherent, the expression of the PSF at a distance $D$ is simplified and reduced to the square module of a 2D Fourier Transform:

$$\mathrm{PSF}(\underline{r}_0) = \frac{1}{D^2\lambda^2 A_M}\left|\int \mathrm{e}^{-\frac{2\pi i}{D\lambda}(\underline{r}\cdot\underline{r}_0)}\, C(\underline{r})\, \mathrm{d}\underline{r}^2\right|^2 \tag{1}$$

where (Figure 4) the integral is extended to the full $\underline{r} = (x, y)$ plane that contains the aperture pupil with ribs and membranes, the screen is described along with the coordinate system $\underline{r}_0 = (x_0, y_0)$, $A_M$ is the clear aperture area (i.e., excluding obstructed locations), and $C(\underline{r})$ is the generalized complex pupil function (CPF), conveying *all* the information on the phase shifts introduced by mirror deformations, misalignments, source setup, plate wedging, and so on. For an SPO MM illuminated by a source at a distance $S$, aligned to the aperture center, we can write the generalized CPF as

$$C(\underline{r}) = \chi_P(\underline{r})\, \mathrm{e}^{-\frac{2\pi i}{\lambda}\left[\frac{R^2}{2f}+\frac{r^2}{2}\left(\frac{1}{f}-\frac{1}{D}-\frac{1}{S}\right)+2\sin\alpha\ \varepsilon(\underline{r})\right]} \tag{2}$$

where the first term in the exponential represents the effect of wedging, i.e., the phase delay introduced by an array of mirrors working in parallel, pointing to the same focus.[9] We dub with $R$ the radii of the plates at the primary-secondary intersection plane, and with $\alpha$ the incidence angles. $R$ takes on discrete values and, due to condition $R = f \tan 4\alpha$, so does $\alpha$. The second term in square brackets allows us to simulate the out-of-focus image when $f \neq D$, and the focus displacement due to the source being at finite distance $S$. As for the third term, we called $\varepsilon(\underline{r})$ the projection of the mirror profile error map $\varepsilon(x_\mathrm{m}, z_\mathrm{m})$ on the $xy$ plane, including misalignments, aberrations due to the source not being on-axis and/or at infinity, and so on, as we will detail in Sect. 4. In this definition, $z_\mathrm{m}$ represents the array of tangential (longitudinal) profiles, and $x_\mathrm{m}$ the array of sagittal (azimuthal) profiles. To a very good approximation, $z_\mathrm{m}$ forms shallow angles $\alpha$ with the $z$-axis. In contrast, $x_\mathrm{m}$ differs from $x$ only by the azimuthal curvatures, which are of the second order and can be neglected here. Finally, $\chi_P$ is the *characteristic function* of the module aperture:

$$\chi_P(\underline{r}) = \begin{cases} 1 & \text{if } \underline{r} \text{ is located on a mirror} \\ 0 & \text{otherwise} \end{cases} \tag{3}$$

In Appendix A we show that Eqs. (1) to (3) immediately entails that i) the PSF is normalized to unity, ii) even if the PSF changes with $\lambda$, its centroid does not. Moreover, we will see in the next sections that the imperfections of the MM *can always be embedded into the error map $\varepsilon$ and the characteristic function $\chi_P$.*

## 3. THE USER INTERFACE OF SWORDS

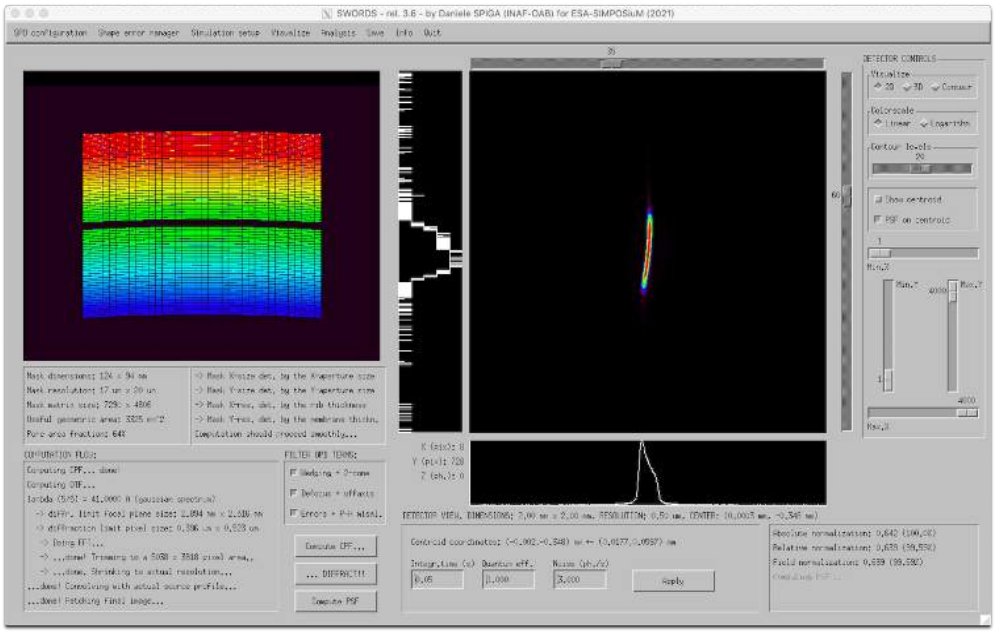


*Figure 5. The main interface of SWORDS, showing the CPF on the left side, with colors depending on the OPD, and the diffracted image at 0.3 keV on the right side, in the presence of a misalignment between the primary and the hyperbolic stacks.*

SWORDS calculates the diffraction pattern of an SPO MM by computing first the OPD map ε, then the CPF using Eq. (2), and finally Eq. (1) for the final result. The main interface, providing access to the OPD map and the diffracted figure, is shown in Figure 5 along with several visualization and analysis tools. However, the first step in the computation is the definition of the SPO MM geometry (Figure 6, left). The user can select the profile (such as a Wolter-I, double cone, or uniform curvature approximation[19]), wedge configuration, focal length, plate radius/size/number, pore/rib/membrane thickness, and so on. The error interface (Figure 6, right) enables the user setting misalignments between the primary and secondary stacks in three rotations and three translations. This can be superimposed to other analytical figure errors, such as curvature radius errors, or single harmonics in the sagittal or the tangential plane. Both amplitudes and phases can be randomized throughout the stacks, with a pseudo-gaussian distribution with an rms value selected by the user (Figure 11, center). The selection can be made independently for the primary and the secondary stack. Another deformation model,[20] mostly acting at the edges of the plates in the tangential and the sagittal direction, can be imparted to the plates. This analytical model (Figure 7) will return a Lorentzian PSF and can be selected in either "even" or "odd" version:[12] both will return the same HEW, but the latter yields an asymmetric PSF. Finally, a 2D polynomial deformation can be superimposed to both stacks, just by entering the coefficients. All these errors get projected on the aperture of the MM to return the total OPD, i.e. the ε(*r*) function used to compute the CPF via Eq. (2).

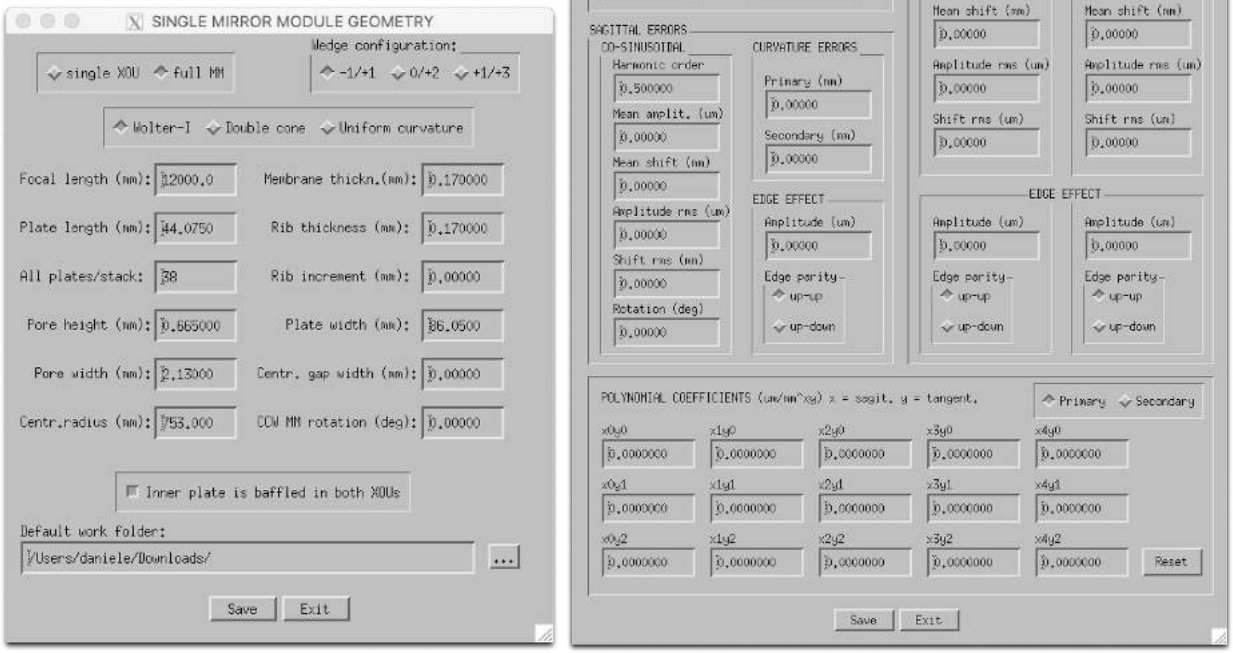


*Figure 6. Left: the input window for the single MM definition. Right: input parameters for modelling analytical profile errors.*

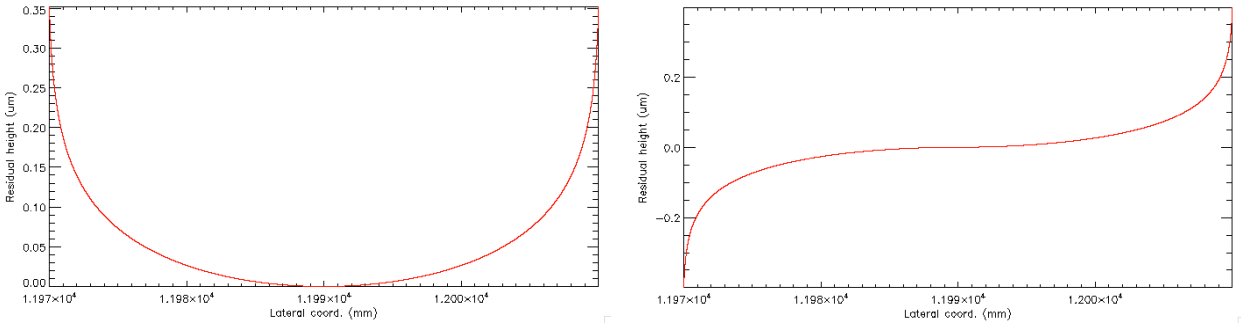


*Figure 7. The profile A log[cos(γx/L)] with γ ≈ π, yielding a Lorentzian PSF. Left: even version. Right: odd version.*

The current version of SWORDS also enables the user to upload a measured error map (the same for all the plates in the MM) or a set of measured error maps (one per plate in the MM). The maps are stretched to fit the plate size; therefore, it is the user's responsibility to make sure that the measurement approximately covers all the plate area. The maps are projected to the exit pupil and resampled to the CPF resolution, then added to the $\varepsilon(\underline{r})$ function to be included into the CPF and so contribute to shape the PSF of the MM.

The user can select the setup for the light source (Figure 8). The possible options for the source include the wavelength $\lambda$ and, to account for the finite monocromaticity of the source, the wavelength bandwidth, which is centered on $\lambda$ and sampled at discrete steps; the program will repeat the computation for every wavelength in the band and then average all the resulting PSFs. This allows the user to get rid of fine diffraction structure that are seldom observed in reality, due to imperfect time coherence of the incident radiation. At the same time, the user can select the size and *S*, the distance of the light source; in this way, the averaged PSF is convolved with the angular size of the source, smoothing out fine diffraction features; this operation also allows the user to account for the finite spatial coherence of the incident radiation. Both the size and the spectrum of the source can be selected in either top-hat or gaussian shape. The source can be placed on-axis or off-axis; this has the effect to change both $\varepsilon(\underline{r})$ by adding an aberration term, and $\chi_P(\underline{r})$ by increasing the rib/membrane obstruction in the MM (see Figure 11, right, and Figure 3, center). When the source goes off-axis, the PSF also moves left-right and/or top-down unless the button "track the source off-axis" is selected. The "Center the focus in MM misalignments" option nulls the global tilt of the OPD, so as to keep the image centered when the primary/secondary stacks are misaligned.

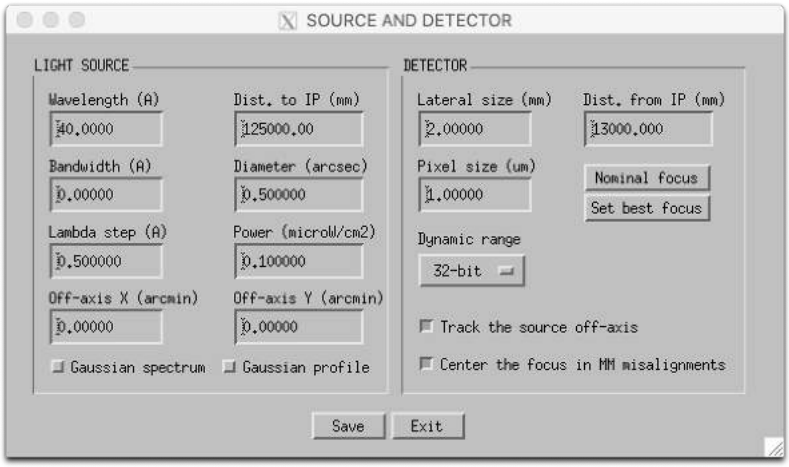


*Figure 8. Input parameters for the source and the detector.*

Finally, the user can select the dimension, the resolution and the dynamic range of the detector (Figure 8). The distance of the MM to the detector, *D*, can be chosen by the user also, with the options of setting it at the nominal focus or at the best focus for the current source distance. The detector size, $F_0$, and its resolution, $\Delta r_0$, respectively affect the resolution $\Delta r$ and the size *F* of the matrix used to map the OPD: in practice, the following constraints are applied by SWORDS when it constructs the CPF:

1. *F* should be at least as large as the maximum size, max(*W*, *H*), of the SPO MM aperture;
2. *F* cannot be *smaller* than $F_{\min} = D\lambda/\Delta r_0$, which equals the size of diffraction fringes from a slit $\Delta r_0$ - wide, at a distance *D;*
3. $\Delta r$ should oversample the minimum thickness of the ribs/membranes in the MM, approx. by a factor of ten;
4. $\Delta r$ cannot be *larger* than $\Delta r_{\max} = D\lambda/F_0$, which equals the size of diffraction fringes from an object $F_0$ - wide, at a distance *D*.

If, at a given $\lambda$, condition 1) is the one that determines *F*, then Eq. (1) will return a PSF with resolution higher than $\Delta r_0$ and the image will be downsampled to the resolution set by the user. Similarly, if condition 3) is the one that determines $\Delta r$ at a given $\lambda$, then Eq. (1) will return a PSF much wider than $F_0$ and the image will be cropped to the size set by the user. If the source is not monochromatic, these conditions are applied for each value of $\lambda$ in the bandwidth. Finally, in order to avoid excessive memory occupancy, the computation is stopped when the detector matrix exceeds $4000 \times 4000$.

## 4. COMPUTING THE COMPLEX PUPIL FUNCTION

In this section, we show some examples of CPFs that can be computed by SWORDS, applying the commands listed in Sect. 3. The CPF can be visualized, decomposed in the various terms that contribute to the functions $\chi_P(\underline{r})$ and $\varepsilon(\underline{r})$ in Eq. (2). For instance, Figure 9 shows the case of a perfect MM of the row 8 in the current optical design of ATHENA (754 mm curvature radius): at left, with the sole $\chi_P(\underline{r})$ visualized: if the "wedging" term is included (the first one in [] of Eq. (2)), we obtain the characteristic figure at center, where the colors mean different OPD values: greater for red, lower for blue. If the detector is out-of-focus, or the source is at finite distance (the second term in [] of Eq. (2)), then the CPF takes the appearance shown at right, where the wavefront at the exit pupil exhibits a clear curvature excess.

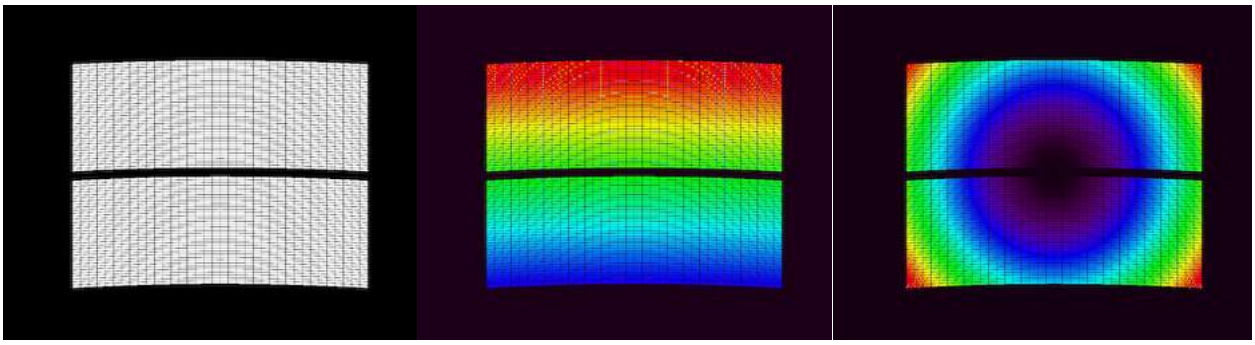

*Figure 9. Left: no OPD terms selected, only ribs and membranes are visible. Center: the wedging term. Right: the defocus term.*

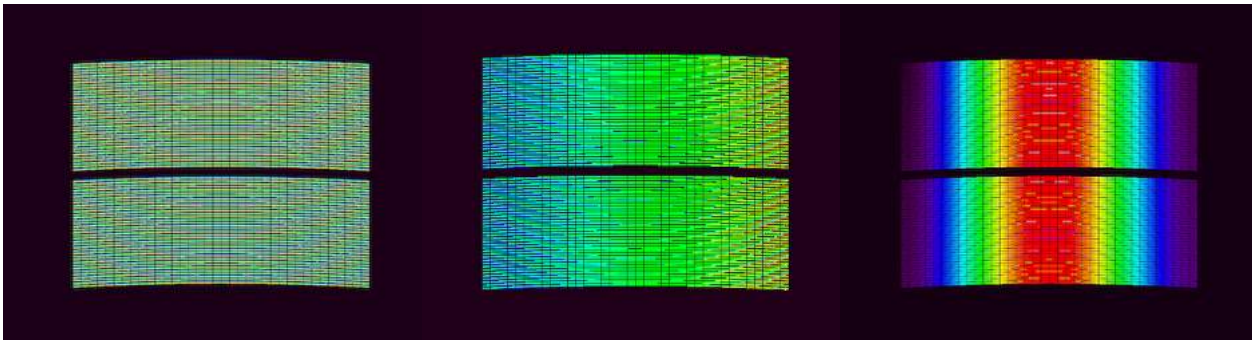

*Figure 10. The misalignment term of the OPD, in the presence of: Left, primary-secondary rotation around the x-axis. Center: a rotation around the y-axis. Right: a sinusoidal error in the sagittal direction.*

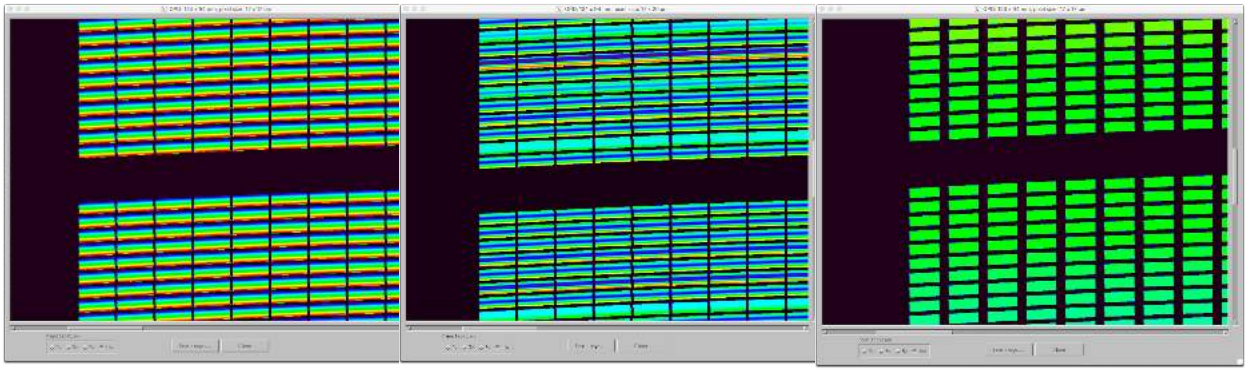

*Figure 11. Detailed view of the OPD with: Left, a sinusoidal error term added to all the plates in the longitudinal direction. Center: sinusoidal errors, with amplitudes and phases randomized from plate to plate. Right: off-axis source by 15 arcmin in the x-axis direction, with a visible increase of the rib vignetting.*

Misalignment between the primary and the secondary stacks are simulated as fictitious figure errors, i.e., taking $\varepsilon(\underline{r})$ as the radial difference between the nominal and the rotated parabolic stacks, and altering $\chi_P(\underline{r})$ to account for the mismatch between ribs and membranes. Rotations about the *x*- and the *y*-axis have a clear effect on the OPD map

(Figure 10, left and center). Sinusoidal errors imparted to the profile along the sagittal are easy to visualize also (Figure 10, right).

Viewing other species of errors, such as errors in the longitudinal direction (Figure 11, left and center), require some magnification of the OPD map, because the profile is compressed by a factor of sinα on the aperture pupil plane. Finally, the right side of Figure 11 shows the OPD map resulting from an off-axis position of the source, which entails an increased rib obstruction, at the expense of the free aperture of the pores. This in turn affects both the collecting area of the MM and its PSF (Figure 3).

## 5. COMPUTING THE DIFFRACTION FIGURE

### 5.1. Perfect modules in X-rays and UV light

Some applications of Eq. (1) to the CPFs shown in Sect. 4 are listed below. In X-rays (Figure 12, left), aperture diffraction effects appear only when the focus is imaged to high magnification and provided that all the figure errors remain negligible. In these conditions, out-of-focus images (Figure 12, center) accurately reproduce the mirror module aperture to-scale. The effect becomes greatly enhanced when the source is brought to a finite distance (Figure 12, right), unless the detector is displaced to follow the focal plane displacement. These results are in qualitative agreement with the outcomes of a ray-tracing routine, with the exception of diffraction fringes.

As opposite to X-rays, the images simulated in UV light (Figure 13) is totally dominated by aperture diffraction and exhibits noticeable diffraction features, both in focus and in extra-focus.

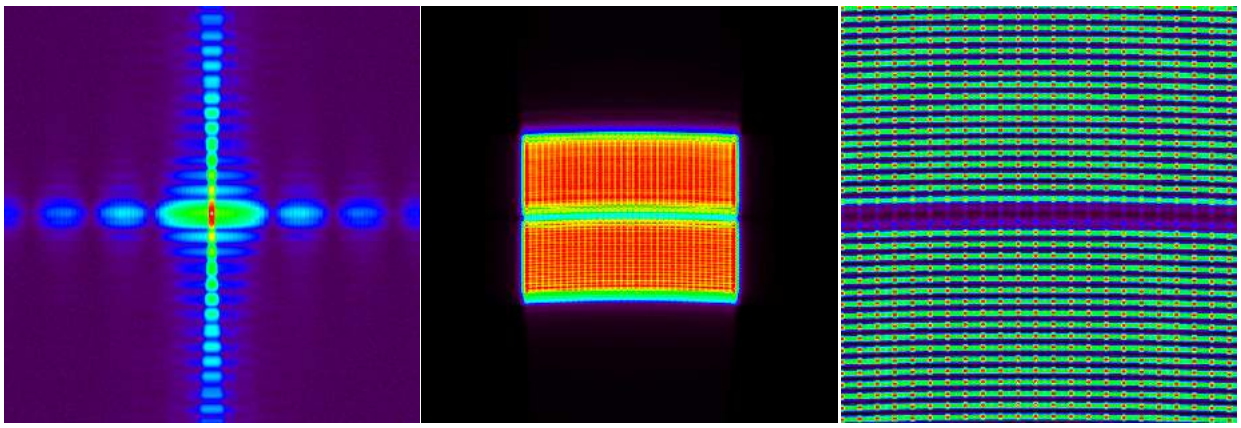

*Figure 12. The focal spot obtained by applying Eq. (1) to the CPF shown in Figure 9, center, at λ = 40 Å, in logarithmic color scale, 2 mm field. The diffraction-limited focal plane is much larger than the detector area (see Sect. 3). Left: source at infinity, detector in the best focus. Center: detector intra-focus by 150 mm. Right: source at a 500 m distance.*

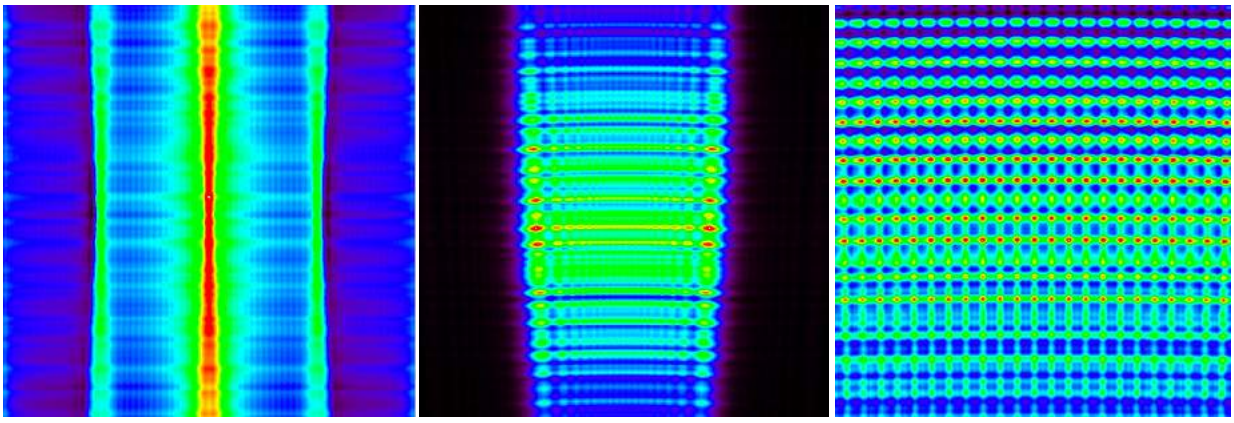

*Figure 13. The simulations of Figure 12, in UV light, λ = (1000 ± 10) Å. This time, the images are dominated by diffraction effects. The color scale is linear. The detector field has been kept to a 2 mm size, for comparison ease with Figure 12, even it would be recommended to scale the detector dimensions in proportion to λ.*

### 5.2. Misaligned primary-secondary stacks

Processing the CPFs of Figure 10 (left and center) via Eq. (1) yields the diffraction figures from an MM with primary and secondary stacks misaligned. A rotation about the *x*-axis returns, as expected, an aberrated image plus a displacement of the focal spot due to the change in the kink angle: this is visible in Figure 14, left, where the image centroid is displaced from the center to $y$ = -0.343 mm. This is equivalent, at a 12 m distance, to a -5.9 arcsec displacement, which is correctly twice the error in the kink angle. In contrast, a rotation about the y-axis (Figure 14, center), causes no centroid displacement but a vertical elongation of the focal spot, another well-known behavior of this kind of misalignments. As expected, the MM is the least sensitive to rotations about the *z*-axis (Figure 14, right), as it takes a 100 arcsec rotation to generate the same lateral displacement (0.364 mm ≈ 100 arcsec × 754 mm) and the aberration coming from just a 3 arcsec rotation about *x*.

Aberrations and displacements can equally be simulated when the primary stack is translated with respect to the secondary one (Figure 15). Along *x* and *y*, the translation mismatches the rib and the membrane positions, increasing the obstruction, and the local curvatures (sagittal along *x*, tangential along *y*) of the reflection points at the plates, causing aberrations. Translation along *z* also causes defocusing (Figure 15, right), but it is the least sensitive misalignment, as it takes order-of-magnitude larger displacements to take effects similar to the other two.

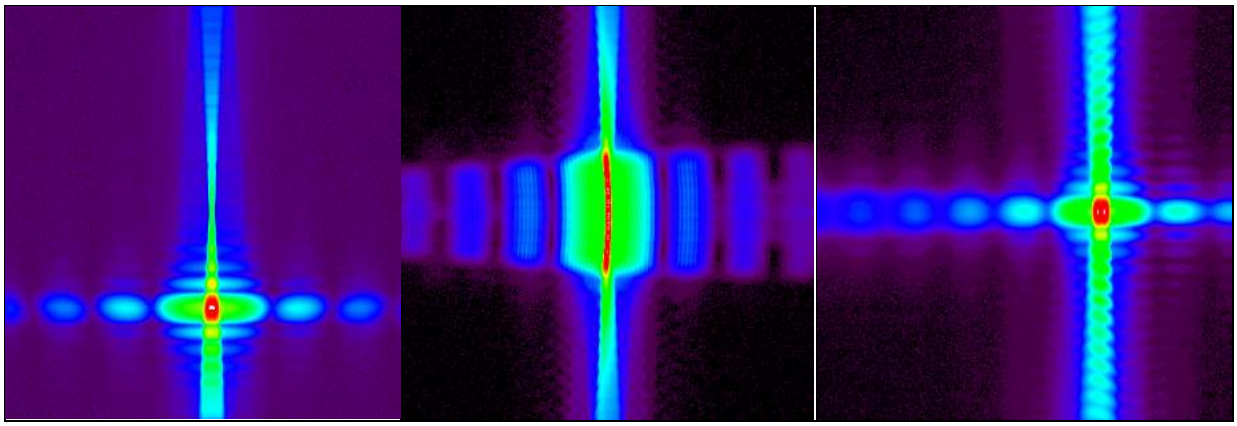

*Figure 14. Simulated PSF of the SPO MM in X-rays λ = 40 Å, in logarithmic color scale, this time with rotations between the primary and the secondary stacks. In order to highlight the spot displacement, the focus centering option was not selected. Left: around the x-axis by 3 arcsec (CPF in Figure 10, left). Center: around the y-axis by 40 arcsec (CPF in Figure 10, center). Right: around the z-axis by 100 arcsec.*

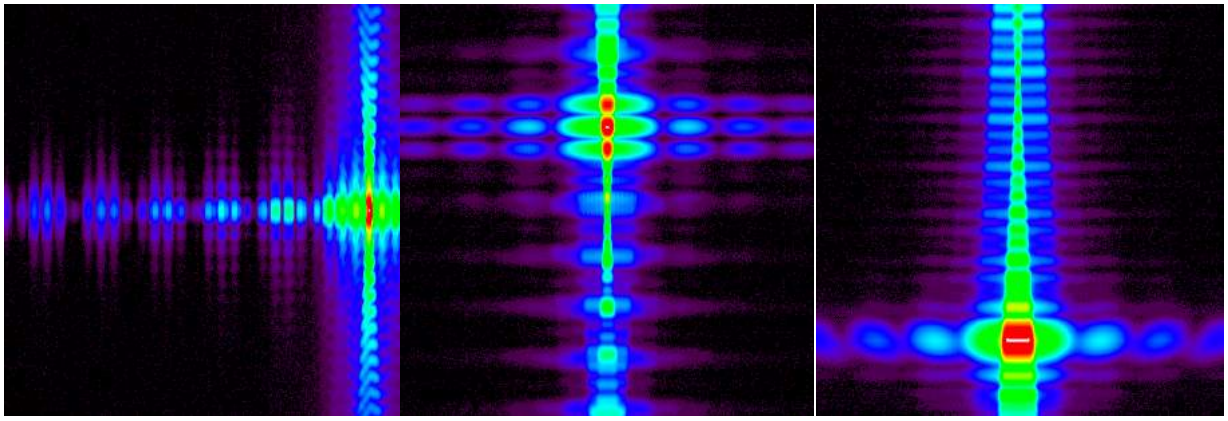

*Figure 15. Simulated PSF of the SPO MM in X-rays λ = 40 Å, in logarithmic color scale, this time with translations between the primary and the secondary stacks. In this case also, the focus centering option was deselected. Left: along the x-axis by +0.75 mm. Center: along the y-axis by 0.4 mm. Right: along the z-axis by 20 mm, toward the source.*

### 5.3. Plate figure errors

Processing CPFs, including sagittal errors, returns the expected aberrations: sinusoidal errors enlarge the focal spot horizontally, but the intensity is not homogeneous because a sinusoid has no constant curvature. For example, a half-

sinusoid like the one modelled in the CPF of Figure 10, right, yields the PSF in Figure 16, left. The bright spots at the two sides are due to the flatness at the two edges of the deformation, while the central curvature makes the reflected ray diverge horizontally (as an example, see the solid line in Figure 18). An error in the sagittal radius of curvature instead causes a uniform elongation of the focal spot along $x$ (Figure 16, center): this kind of error makes the optic astigmatic, because the sagittal focus is displaced closer to / farther from the MM. In the case hereby shown (Figure 16, right) the sagittal radius is increased by 7.5 mm and the sagittal focus is - correctly - placed 119 mm away, even if it does no longer coincide with the tangential focus.

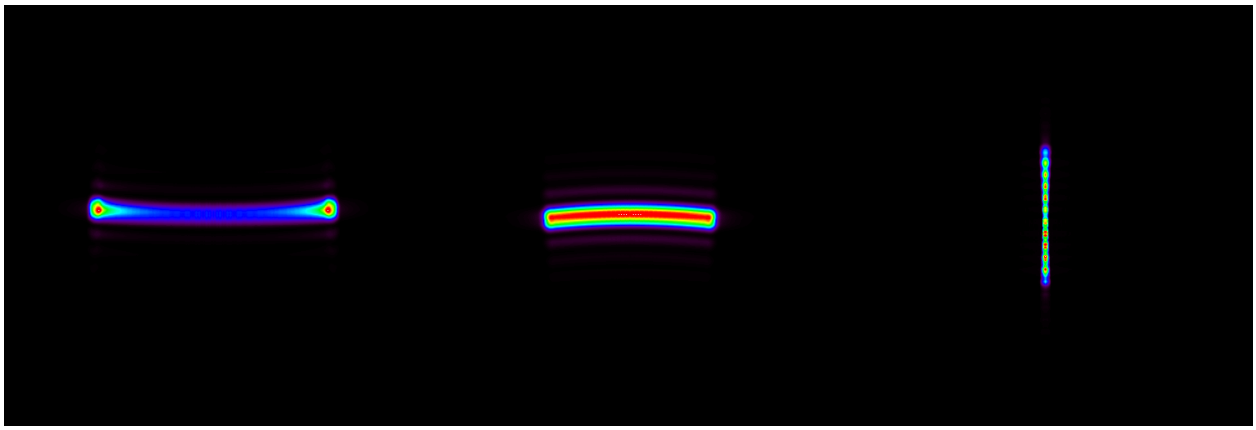

*Figure 16. Simulation at $l$ = 40 Å, 2 mm field, of the MM with a sagittal error in each plate, with constant phase and amplitudes. Linear color scale. Left: period equal to twice the plate width and a 20 μm amplitude. Center: +7.5 mm curvature radius error, in the nominal focus. Right: focal plane re-focused, placed as expected, at 7.5/754 × 12000 mm = 119 mm beyond the nominal focus.*

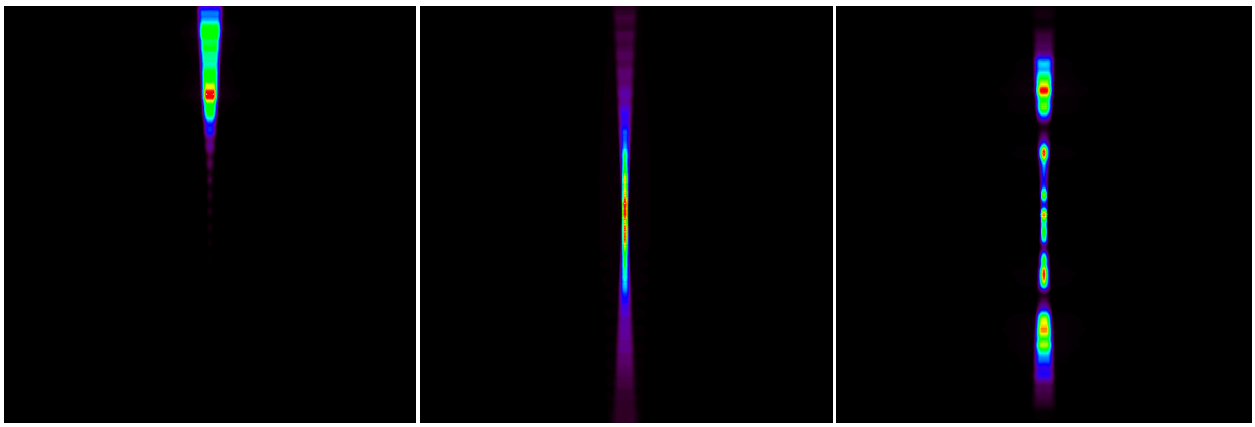

*Figure 17. Simulated PSF of the SPO MM in X-rays $\lambda$ = 40 Å, in linear color scale, in the presence of: Left, a double-cone profile instead of a Wolter-I. Center, a 1 μm-ample edge lifting along the plate length, yielding a Lorentzian PSF.[20] Right, a 0.1 μm-ample sinusoidal deformation with a period equal to the plate length (44 mm), at 0.5 keV.*

Tangential errors sometimes return the expected PSF. For example, adding the cone-parabola difference to $\varepsilon(\underline{r})$ nulls the tangential focus, because the cone has no focusing capabilities. This is visible in Figure 17, left, where the focus is elongated by an amount equal to the pore height. The vertical displacement is due to the cone being tangent to the parabola/hyperbola at the kink angle, and not in its mid-point. Also adding the "even" analytical profile displayed in Figure 7, left, returns the expected result of a Lorentzian PSF.[20] The "odd" version of the profile would instead return a totally asymmetric PSF.

However, some profiles do not behave as per the geometric optic expectations. An example is the diffraction figure obtained from a half-sinusoid figure error along the tangential direction, which yields a multiple-peak pattern (Figure 17, right) rather than the two-peaked PSF that one would expect from geometric optics, and that would resemble Figure 16, left, only oriented in vertical. SWORDS provides, indeed, a picture in excellent agreement with the 1D predictions of the WISE program[1] and with those of the sinusoidal grating theory (Figure 18). The reason of the difference is that the amplitude of the tangential defect is much lower than the sagittal one, which makes the OPD

much lower despite the similar extent of the PSF, so that the separation between diffraction orders becomes much more evident. The geometric optic PSF is, in reality, the superposition of a number of high-order diffraction peaks, which cannot be resolved individually with a realistic pixel size; we would obtain it either simulating at higher energies, or assuming defects with much greater amplitude.[1]

## 6. CONCLUSIONS

In this paper, we have presented the capabilities of the SWORDS program, developed in the context of the SImPOSIUM project. The program enables an easy, fast and reliable simulation of the diffraction pattern in an SPO mirror module, also accounting for imperfections and misalignments, and applicable from UV to soft X-rays. Showing SWORDS capabilities also provided us with the opportunity to demonstrate the versatility of wave optics in solving the problem of predicting the PSF of an SPO MM, accounting for aperture diffraction and figure errors in a self-consistent manner. Future extensions of this work will be aimed at modelling diffraction and interference from groups of SPO MMs.

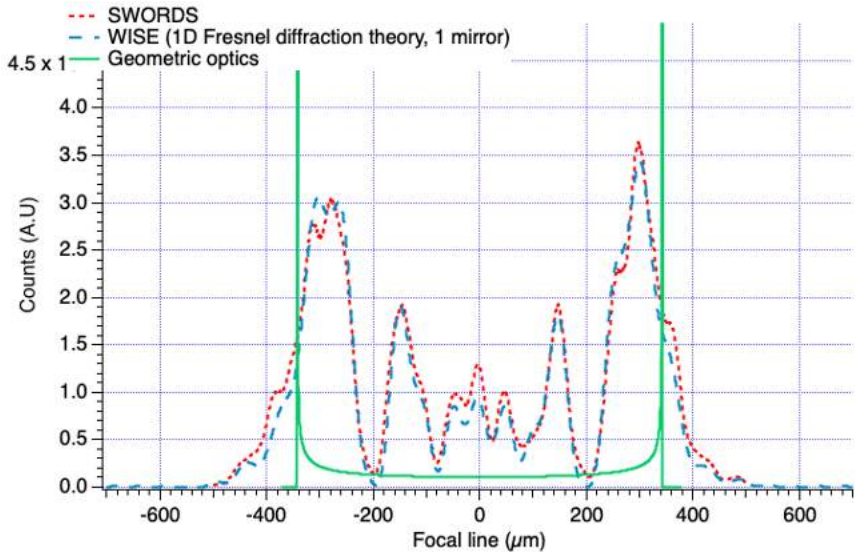


*Figure 18. The projection of the PSF in Figure 17, right, along the y-axis (dotted line) is in excellent agreement with the 1D expectations of the WISE simulation program (dashed line)[1] and in net disagreement with those of geometrical optics (solid line).[20] The multiple fringes are typical features of a sinusoidal grating.*

## APPENDIX A. PROOF OF THE PSF CENTROID INVARIANCE

In Sect. 2, we concluded that in single diffraction, Fresnel approximation, the PSF of a SPO MM at the light wavelength λ, seen on a screen mapped by the coordinates $\underline{r}_0$ (Figure 4) at a distance equal to the focal length, $f$, can be computed via Eq. (1), with $D = f$, $S \to \infty$,

$$\mathrm{PSF}(\underline{r}_0) = \frac{1}{f^2\lambda^2 A_M}\left|\int \mathrm{e}^{-\frac{2\pi i}{f\lambda}(\underline{r}\cdot\underline{r}_0)}\, C(\underline{r})\, \mathrm{d}\underline{r}^2\right|^2 \tag{A.1}$$

where $C(\underline{r})$ is the in-focus generalized CPF (Eq. (2), refer to Sect. 2 for the explanation of symbols):

$$C(\underline{r}) = \chi_P(\underline{r})\, \mathrm{e}^{-\frac{2\pi i}{\lambda}\left[\frac{R^2}{2f}+2\sin\alpha\, \varepsilon(\underline{r})\right]} \tag{A.2}$$

We now aim at an expression for the PSF centroid coordinates, at any value of λ. To this end, with the aid of the Wiener-Khintchine theorem, we rewrite Eq. (A.1) in a different form:

$$\mathrm{PSF}(\underline{r}_0) = \frac{1}{f^2\lambda^2}\int \mathrm{e}^{-\frac{2\pi i}{f\lambda}\left(\underline{\xi}\cdot\underline{r}_0\right)}\hat{C}\left(\underline{\xi}\right)\mathrm{d}\underline{\xi}^2 \tag{A.3}$$

being $\hat{C}\left(\underline{\xi}\right)$ the autocorrelation function of $C(\underline{r})$,

$$\hat{C}\left(\underline{\xi}\right) = \frac{1}{A_M}\int C(\underline{r})\ C^*\left(\underline{r}+\underline{\xi}\right)\mathrm{d}\underline{r}^2 \tag{A.4}$$

where * means complex conjugation, and $\underline{\xi} = (\xi_x, \xi_y)$ is the "lag" in $xy$. It is easily proven that the PSF is normalized to 1, on condition that the detector field $F$ be wide enough to fully enclose it, so as to allow us assuming $F \to \infty$:

$$\begin{aligned}\int \mathrm{PSF}(\underline{r}_0)\,\mathrm{d}\underline{r}_0^2 &= \frac{1}{f^2\lambda^2}\int \mathrm{d}\underline{\xi}^2\ \hat{C}\left(\underline{\xi}\right)\int \mathrm{d}\underline{r}_0^2\ \mathrm{e}^{-\frac{2\pi i}{f\lambda}\left(\underline{\xi}\cdot\underline{r}_0\right)} = \frac{1}{f^2\lambda^2}\int \mathrm{d}\underline{\xi}^2\ \hat{C}\left(\underline{\xi}\right)\lim_{F_0\to\infty}\int_{-\frac{F_0}{2}}^{+\frac{F_0}{2}}\mathrm{d}\underline{r}_0^2\,\mathrm{e}^{-\frac{2\pi i}{f\lambda}\left(\underline{\xi}\cdot\underline{r}_0\right)} = \\ &= \int \mathrm{d}\underline{\xi}^2\hat{C}\left(\underline{\xi}\right)\delta\left(\underline{\xi}\right) = \hat{C}(\underline{0}) = \frac{1}{A_M}\int\left|C(\underline{r})\right|^2\mathrm{d}\underline{r}^2 = \frac{1}{A_M}\int \chi_P^2(\underline{r})\,\mathrm{d}\underline{r}^2 = 1\end{aligned} \tag{A.5}$$

To get the projection of the PSF on the $y_0$ axis, we firstly integrate Eq. (A.3) over $x_0$:

$$\begin{aligned}\mathrm{PSF}(y_0) &= \frac{1}{f^2\lambda^2}\int \mathrm{d}x_0\int \mathrm{d}\underline{\xi}^2\ \hat{C}\left(\underline{\xi}\right)\ \mathrm{e}^{-\frac{2\pi i}{f\lambda}\left(\underline{\xi}\cdot\underline{r}_0\right)} = \frac{1}{f^2\lambda^2}\int \mathrm{d}\underline{\xi}^2\ \hat{C}\left(\underline{\xi}\right)\mathrm{e}^{-\frac{2\pi i}{f\lambda}y_0\xi_y}\int \mathrm{d}x_0\ \mathrm{e}^{-\frac{2\pi i}{f\lambda}x_0\xi_x} = \\ &= \frac{1}{f\lambda}\int \mathrm{d}\underline{\xi}^2\ \hat{C}\left(\underline{\xi}\right)\mathrm{e}^{-\frac{2\pi i}{f\lambda}y_0\xi_y}\,\delta(\xi_x) = \frac{1}{f\lambda}\int \mathrm{d}\xi_y\ \hat{C}(0,\xi_y)\ \mathrm{e}^{-\frac{2\pi i}{f\lambda}y_0\xi_y}\end{aligned} \tag{A.6}$$

We now apply the definition of PSF centroid, starting from the $y_0$-coordinate:

$$y_c = \int y_0\ \mathrm{PSF}(y_0)\ \mathrm{d}y_0 = \frac{1}{f\lambda}\int \mathrm{d}y_0\int \mathrm{d}\xi_y\ \hat{C}_y(\xi_y)\ y_0\mathrm{e}^{-\frac{2\pi i}{f\lambda}y_0\xi_y} \tag{A.7}$$

where we have set $\hat{C}(0,\xi_y) = \hat{C}_y(\xi_y)$ to abridge the notation. Then, integrating by parts and recalling that $\hat{C}_y \to 0$ when $|\xi_y| \to \infty$, we easily dispose of the factor $y_0$ and remain with

$$y_c = \frac{1}{2\pi i}\int \mathrm{d}y_0\int \mathrm{d}\xi_y\frac{\partial\hat{C}_y}{\partial\xi_y}\ \mathrm{e}^{-\frac{2\pi i}{f\lambda}y_0\xi_y} \tag{A.8}$$

Equation (A.8) is easily solved by just switching the integration order:

$$y_c = \frac{1}{2\pi i}\int \mathrm{d}\xi_y\frac{\partial\hat{C}_y}{\partial\xi_y}\int \mathrm{d}y_0\ \mathrm{e}^{-\frac{2\pi i}{f\lambda}y_0\xi_y} = \frac{f\lambda}{2\pi i}\int \mathrm{d}\xi_y\frac{\partial\hat{C}_y}{\partial\xi_y}\ \delta(\xi_y) = \frac{f\lambda}{2\pi i}\frac{\partial\hat{C}_y}{\partial\xi_y}(0) \tag{A.9}$$

Taking the derivative of Eq. (A.4) with respect to $\xi_y$, and integrating by parts, we now get

$$\begin{aligned}\frac{\partial\hat{C}_y}{\partial\xi_y}(\xi_y) &= \frac{1}{A_M}\int C(x,y)\ \frac{\partial C^*}{\partial\xi_y}(x,y+\xi_y)\,\mathrm{d}\underline{r}^2 = -\frac{1}{A_M}\int \frac{\partial C^*}{\partial\xi_y}(x,y)\ C^*(y+\xi_y)\,\mathrm{d}\underline{r}^2 = \\ &= -\frac{1}{A_M}\int \frac{\partial C^*}{\partial\xi_y}(x,y-\xi_y)\ C^*(y)\,\mathrm{d}\underline{r}^2 = -\frac{\partial\hat{C}_y^*}{\partial\xi_y}(-\xi_y)\end{aligned} \tag{A.10}$$

and the derivative of $\hat{C}_x$ with respect to $\xi_x$ has the same symmetry properties. This means that the real part of the gradient of $\hat{C}$ along is an odd function along both axes, which implies that $\mathrm{Re}\left[\underline{\nabla}\hat{C}(\underline{0})\right] = 0$. Moreover, a totally similar reasoning can be repeated for $x_c$, the $x_0$-coordinate of the centroid, so we have a succinct expression for $\underline{r}_c = (x_c, y_c)$:

$$\underline{r}_c = \frac{f\lambda}{2\pi i}\ \mathrm{Im}\left[\underline{\nabla}\hat{C}(\underline{0})\right] \tag{A.11}$$

which is, clearly, a real vector. Let us now apply this general result to our case, i.e., to the generalized CPF of an SPO MM. Substituting Eq. (A.2) into Eq. (A.4) with $\xi_x = 0$ then returns:

$$\hat{C}_y(\xi_y) = \frac{1}{A_M}\int \chi_P(x,y)\ \chi_P(x,y+\xi_y)\ \mathrm{e}^{-\frac{4\pi i}{\lambda}\sin\alpha[\varepsilon(x,y)-\varepsilon(x,y+\xi_y)]}\,\mathrm{d}\underline{r}^2 \tag{A.12}$$

where the terms depending on $R$ have been dropped, because their values remain constant in the vicinities of $\xi_y = 0$ and will cancel out in the subsequent gradient operation (Eq. (A.14)). A result analogous to Eq. (A.12) holds along $x$,

$$\hat{C}_x(\xi_x) = \frac{1}{A_M}\int \chi_P(x,y)\,\chi_P(x+\xi_x,y)\,\mathrm{e}^{-\frac{4\pi i}{\lambda}\sin\alpha[\varepsilon(x,y)-\varepsilon(x+\xi_x,y)]}\,\mathrm{d}\underline{r}^2 \tag{A.13}$$

and so, the gradient of $\hat{C}$ at $\underline{\xi} = 0$ can be easily calculated as

$$\underline{\nabla}\hat{C}(\underline{0}) = \frac{1}{A_M}\int \chi_P\,\underline{\nabla}\chi_P\,\mathrm{d}\underline{r}^2 + \mathrm{i}\frac{4\pi}{\lambda A_M}\int \chi_P^2\,\underline{\nabla}\varepsilon\,\sin\alpha\,\mathrm{d}\underline{r}^2 \tag{A.14}$$

then combining this result with Eq. (A.11), we remain with

$$\underline{r_c} = \frac{2f}{A_M}\int \chi_P^2\,\underline{\nabla}\varepsilon\,\sin\alpha\,\mathrm{d}\underline{r}^2 \tag{A.15}$$

Now, since in grazing incidence we have $\sin\alpha \approx \tan\alpha = \partial y/\partial z_\mathrm{m}$, the derivative of the mirror profiles in the tangential direction, we can write the $y_0$ component of the centroid as

$$y_c \approx \frac{2f}{A_M}\int \chi_P^2\frac{\partial\varepsilon}{\partial y}\frac{\partial y}{\partial z_m}\mathrm{d}\underline{r}^2 = \frac{2f}{A_M}\int \chi_P^2\frac{\partial\varepsilon}{\partial z_m}\mathrm{d}\underline{r}^2 = 2f\left\langle\frac{\partial\varepsilon}{\partial z_m}\right\rangle \tag{A.16}$$

where we have made use of the chain rule for derivation and the $\langle\ \rangle$ brackets denote average of the tangential error slope. Equation (A.16) exactly returns the position expected from the geometrical optics at a distance $f$. As for the $x_0$ component, we can write similar passages, but this time we have $x \approx x_\mathrm{m}$; therefore, we obtain

$$x_c \approx \frac{2f}{A_M}\int \sin\alpha\,\chi_P^2\frac{\partial\varepsilon}{\partial x}\mathrm{d}\underline{r}^2 \approx \frac{f}{A_M}\int \sin 2\alpha\,\chi_P^2\frac{\partial\varepsilon}{\partial x_m}\mathrm{d}\underline{r}^2 = f\left\langle\sin 2\alpha\frac{\partial\varepsilon}{\partial x_m}\right\rangle \tag{A.17}$$

This confirms that the transverse displacement of the centroid depends on the average value of the sagittal error slope, but it is mitigated by a factor of sinα with respect to tangential errors, a well-known result in grazing-incidence optics. We can so conclude that the coordinates of the centroid are independent of $\lambda$ and coincide with the position expected from geometrical optics.

## ACKNOWLEDGMENTS

The "SIlicon Pore Optics SImUlation and Modelling" project (SImPOSIUM) is supported by the European Space Agency (contract number 4000114410).

## REFERENCES

[1]. Raimondi, L., Spiga, D., "Mirrors for X-ray telescopes: Fresnel diffraction-based computation of point spread functions from metrology," Astronomy and Astrophysics, Vol. 573, A22 (2015)
[2]. Spiga, D., Raimondi, L., "X-ray optical systems: from metrology to Point Spread Function," Proc. SPIE 9209, 92090E (2014)
[3]. Rebuffi, L., Sanchez Del Rio, M., "OASYS (OrAnge SYnchrotron Suite): an open-source graphical environment for x-ray virtual experiments," Proc. SPIE 10388, 103880S (2017)
[4]. Bavdaz, M., Wille, E., Ayre, M., Ferreira, I., Shortt, B., Fransen, S., Millinger, M., Collon, M., Vacanti, G., Barrière, N., Landgraf, B., et al., "ATHENA optics technology development," Proc. SPIE 12181, this conference
[5]. Collon M. J., Abalo, L., Babic, L., Barrière, N. M., Bayerie, A., Castiglione, L., Eenkhoorn, N., Girou, D., Günther, R., Hauser, E., et al., "The development of the mirror for the Athena X-ray mission," Proc. SPIE 12181, this conference
[6]. Salmaso, B., Basso, S., Ghigo, M., Spiga, D., Vecchi, G., Sironi, G., Cotroneo, V., Conconi, P., Redaelli, E., Bianco, A., Pareschi, G., Tagliaferri, G., Sisana, D., et al., "X-ray tests of the ATHENA mirror modules in BEaTriX: from design to reality," Proc. SPIE 12181, this conference

[7]. Valsecchi, G., Vernani, D., Marioni, F., Zocchi, F, Bianucci, G., "Alignment and integration of the SPO mirror modules onto the ATHENA telescope," Proc. SPIE 12181, this conference
[8]. Moretti, A., Pareschi, G., Basso, S., Spiga, D., Ghigo, M., Sironi, G., Tagliaferri, G., Civitani, M., Cotroneo, V., La Palombara, N., Uslenghi, M., Tordi, M., Delorenzi, S., Dury, F., Valsecchi, G., Zocchi, F., Marioni, F., Vernani, D., Amisano, F., Parissenti, G., Parodi, G., Ottolini, M., Corradi, P., Bavdaz, M., Ferreira, I., "The VERT-X calibration facility: development of the most critical parts," SPIE Proc. 11822 118220K (2021)
[9]. Spiga, D., Christensen, F. E., Bavdaz, M., Civitani, M., Conconi, P., Della Monica Ferreira, D., Bergbäck Knudsen, E., Massahi, S., Pareschi, G., Salmaso, B., Shortt, B., Tayabaly, K., Westergaard, N., Wille, E., "Simulation and modeling of silicon pore optics for the ATHENA x-ray telescope," Proc. SPIE 9905, 99055O (2016)
[10]. Sironi, G., Spiga, D., Moretti, A., Pareschi, G., Tagliaferri, G., Della Monica Ferreira, D., Bergbäck Knudsen, E., 'S Jegers, A., Ferreira, I., Bavdaz, M., "Open-source simulator for ATHENA X-ray telescope optics," Proc. SPIE 11822, 118220I (2021)
[11]. 'S Jegers, A., Della Monica Ferreira, D., Bergbäck Knudsen, E., Massahi, S., Svendsen, S., Gellert, N. C., Sironi, G., Spiga, D., Ferreira, I., Bavdaz, M., Vacanti, G., Madsen, K. K., "The effect of curvature and wedging on the angular resolution of Athena," Proc. SPIE 12181, this conference
[12]. Spiga, D., "SWORDS – SoftWare fOR Diffraction Simulation of silicon pore optics: the user manual," INAF-OAB internal report 06/2021 – http://dx.doi.org/10.13140/RG.2.2.22411.36647
[13]. Mieremet, A.L., Beijersbergen, M.W., "Fundamental spatial resolution of an x-ray pore optic," Appl. Opt. 44(33), 7098 (2005)
[14]. Friedrich, P., Bräuninger, H., Budau, N., Burkert, W., Eder, J., Freyberg, M., Hartner, G., Mühlegger, M., Predehl, P., Erhard, M., Gutruf, F., Jugler, D., Kampf, D., et al., "Design and development of the eROSITA x-ray mirrors," Proc. SPIE 7011, 70112T (2008)
[15]. Valsecchi, G., Marioni, F., Bianucci, G., Zocchi, F. E., Gallieni, D., Parodi, G., Ottolini, M., Collon, M., Pareschi, G., Spiga, D., Bavdaz, M., Wille, E., Burwitz, V., "Results of silicon pore optics mirror modules optical integration in the ATHENA telescope," Proc. SPIE 10699, 106990Z (2018)
[16]. Spiga, D., Della Monica Ferreira, D., Shortt, B., Bavdaz, M., Bergbäck Knudsen, E., Bianucci, G., Christensen, F., Civitani, M., Collon, M., Conconi, P., Fransen, S., et al., "Optical simulations for design, alignment, and performance prediction of silicon pore optics for the ATHENA x-ray telescope," Proc. SPIE 10399, 103990H (2017)
[17]. Spiga, D., Cocco, D., Hardin, C., Morton, D., Ng, M.L., "Simulating the optical performances of the LCLS bendable mirrors using a 2D physical optics approach," Proc. SPIE, 10761, 1076107 (2018)
[18]. Spiga, D., Moretti, A., Pareschi, G., Sironi, G., Tagliaferri, G., Bavdaz, M., Ferreira, I., Valsecchi, G., Marioni, F., Zocchi, F., "Optical simulations for the Wolter-I collimator in the VERT-X calibration facility," Proc. SPIE 11822 (2021)
[19]. Willingale, R., Spaan, R., "Improving the angular resolution of the conical Wolter-I silicon pore optics (SPO) mirror design for the International X-ray Observatory (IXO)," Proc. SPIE 7732, 773241 (2010)
[20]. Spiga, D., Raimondi, L., Svetina, C., Zangrando, M., "X-ray beam-shaping via deformable mirrors: Analytical computation of the required mirror profile," NIM-A 710, 125–130 (2013)